# Magnetoresistance anomaly during the electrical triggering of a metal-insulator transition

Pavel Salev [1], Lorenzo Fratino [2,3] Dayne Sasaki [4], Soumen Bag,[2] Yayoi Takamura [4],
Marcelo Rozenberg [2], and Ivan K. Schuller[5]

[1]*Department of Physics & Astronomy, University of Denver, Denver, Colorado 80210, USA*
[2]*Université Paris-Saclay, CNRS Laboratoire de Physique des Solides, 91405 Orsay, France*
[3]*Laboratoire de Physique Théorique et Modélisation, CNRS UMR 8089, CY Cergy Paris Université, 95302 Cergy-Pontoise Cedex, France*
[4]*Department of Materials Science and Engineering, University of California Davis, Davis, California 95616, USA*
[5]*Department of Physics and Center for Advanced Nanoscience, University of California San Diego, La Jolla, California 92093, USA*

Phase separation naturally occurs in a variety of magnetic materials and it often has a major impact on both electric and magnetotransport properties. In resistive switching systems, phase separation can be created on demand by inducing local switching, which provides an opportunity to tune the electronic and magnetic state of the device by applying voltage. Here we explore the magnetotransport properties in the ferromagnetic oxide $La_{0.7}Sr_{0.3}MnO_3$ (LSMO) during the electrical triggering of an intrinsic metal-insulator transition (MIT), which produces volatile resistive switching. This switching occurs in a characteristic spatial pattern, i.e., the formation of a high-resistance barrier perpendicular to the current flow, enabling an electrically actuated ferromagnetic-paramagnetic-ferromagnetic phase separation. At the threshold voltage of the MIT triggering, both anisotropic and colossal magnetoresistances exhibit anomalies including a large increase in magnitude and a sign flip. Computational analysis revealed that these anomalies originate from the coupling between the switching-induced phase separation state and the intrinsic magnetoresistance of LSMO. This work demonstrates that driving the MIT material into an out-of-equilibrium resistive switching state provides the means for electrical control of the magnetotransport phenomena.

## I. INTRODUCTION

Resistive switching electronics and spintronics emerged as two leading frameworks for the development of scalable and energy-efficient memories and signal processing devices for next generation information technologies [1–3]. In resistive switching systems, an electric stimulus, voltage or current, programs the material's resistivity either in a volatile or non-volatile way [4]. In spintronics, electrical signals are used to manipulate and probe the magnetic degrees of freedom [5]. Combining resistive switching and spintronic functionalities in a single device presents an exciting opportunity to bring together the advantages of charge- and spin-based electronics, enriching the design space for practical applications, and to further the basic understanding of the interactions between electrical and magnetic phenomena in materials.

A common mechanism of the nonvolatile resistive switching is the electrically induced ionic migration [6]. The application of voltage to a metal-insulator-metal heterostructure can drive ion diffusion from the metal electrodes into the insulator layer [5] or cause the ion rearrangement within the insulator [7], leading to a change of the heterostructure's resistance. When a magnetic material is incorporated into an ionic migration device, inducing the resistive switching can enable the electrical control of magnetic properties such as anisotropic and tunneling magnetoresistances [8–14], saturation magnetization [15–17], exchange bias [18,19], and magnetic domain configuration [20,21].

The application of an electric stimulus to a material featuring a metal-insulator transition (MIT) can produce a large resistance change without the ionic migration [4]. Typically, the applied voltage/current drives the MIT material across the phase transition either by Joule heating or by field-induced carrier doping [22–24]. Electrical triggering of the MIT results in a volatile resistive switching, i.e., a switching that automatically resets upon the removal of the electrical stimulus. Volatile MIT switching is actively being pursued in applications including selectors in crossbar arrays [25,26], rf and optoelectronics switches [27–29], and spiking oscillators for neuromorphic [30–33] and stochastic [34,35] computing. Because of the volatility, the MIT switching is not directly applicable in memories, although several works have demonstrated nonvolatile memristive functionalities in the MIT devices by utilizing the hysteretic first order transitions [36–38], ramp-reversal memory [39,40], and artificial heterostructures [41,42].

While the electrical properties in the MIT switching devices have been studied extensively, the magnetic functionalities remain largely unexplored despite the fact that many MIT materials also have magnetic ordering [43]. For example, MIT switching has been reported in several magnetic rare-earth manganites [44,45], but the influence of this MIT switching on phenomena such as magnetotransport is still unknown, as the research on achieving electrical control of magnetic properties in manganites is primarily focused on using electrostatic gating [46], magnetoelectric heterostructures [47], spin-torques [48], etc. During the electrical MIT triggering, a different electronic and magnetic phase is locally injected into the otherwise homogeneous material, often due to the formation of a percolating filament [49] or
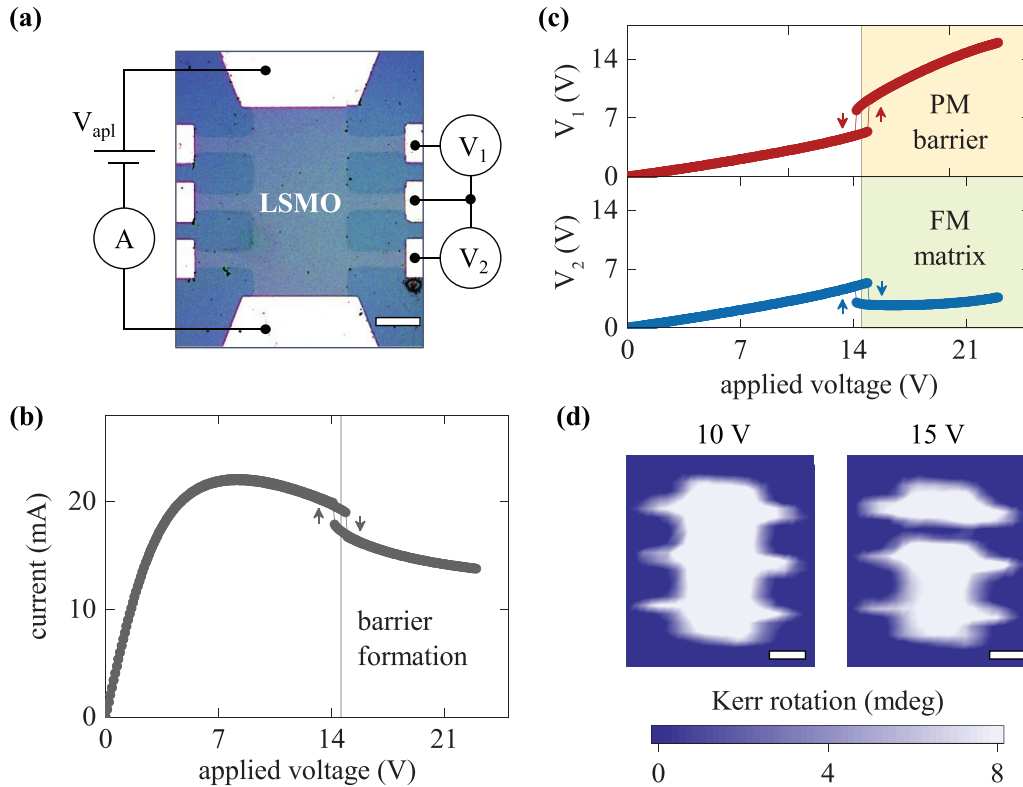
174434-1

**(a)**

**(b)**

**(c)**

**(d)**



FIG. 1. (a) Schematic of the resistive switching measurement setup. Optical image shows a $50 \times 100\,\mu m^2$ LSMO Hall bar device. Scale bar is 25 μm. (b) Global *I-V* curve of the LSMO Hall bar showing the volatile low-to-high resistance switching. (c) Local voltages across the Hall bar arms recorded during the switching. At the 14.5-V threshold voltage, local voltage $V_1$ across the top Hall bar section abruptly increases indicating the low-to-high resistance switching. (d) MOKE maps of the Hall bar recorded under the applied voltage of 10 V (left) and 15 V (right). While the 10-V map is uniformly ferromagnetic, the 15-V map shows the formation of a PM barrier in the top section indicating the local MIT triggering. Scale bars are 25 μm. All measurements were performed at 100 K.

transverse barrier [50]. It can be expected that the electrically induced phase separation can influence magnetic ordering similar to the naturally occurring phase separation in magnetic materials [51]. Electrical control of the phase separation by the MIT switching can enable the electrical manipulation of magnetic properties without altering the material's chemical composition as in the case of ionic-migration systems. Recently, we reported magneto-optical studies of the uniaxial magnetic anisotropy emerging in a ferromagnetic MIT oxide La$_{0.7}$Sr$_{0.3}$MnO$_3$ (LSMO) when the applied voltage induces volatile resistive switching [52]. In this work, we focus on the magnetotransport properties during the electrical triggering of MIT in LSMO. Because the MIT triggering in LSMO is mediated by Joule heating, one might expect that the magnetoresistance properties when the material undergoes the MIT switching would be similar to those in thermal equilibrium. We observed, however, strong anomalies both in anisotropic and colossal magnetoresistances (AMR and CMR), including a large change in magnitude and sign flip of the magnetoresistance. We attributed these magnetotransport anomalies to the coupling between the switching driven paramagnetic/ferromagnetic (PM/FM) phase separation (formation of the hot high-resistance PM phase barrier that splits the cold low-resistance FM matrix) and intrinsic magnetoresistance of LSMO. Natural phase separation is a well-known phenomenon that has a major impact on magnetotransport

in many magnetic rare-earth manganites [53]. Even though LSMO with the La:Sr ratio of 0.7:0.3 does not exhibit a phase separation in equilibrium, local electrical MIT triggering allows creating an artificial FM/PM phase separation pattern that, as we show here, causes an anomalous magnetoresistance behavior. Our findings provide a unique perspective on the role of nonequilibrium phase separation in determining the AMR and CMR of LSMO and introduces an unconventional approach to control the spin-dependent transport in magnetic MIT materials that are driven out of equilibrium by strong electrical stimuli.

## II. METAL-INSULATOR TRANSITION SWITCHING

We studied the impact of electrical MIT triggering on the magnetotransport properties using the standard Hall bar geometry devices [optical image in Fig. 1(a)]. The devices were patterned in a 20-nm-thick La$_{0.7}$Sr$_{0.3}$MnO$_3$ film epitaxially grown on a (001)-oriented SrTiO$_3$ substrate [54,55]. The Hall bars were aligned with the [100] crystallographic direction. Under equilibrium conditions, i.e., at voltages/currents far below the switching threshold, the resistance-temperature measurements showed a phase transition between the low-resistance FM metal and high-resistance PM metal at $T_c \sim$ 345 K (see Supplemental Material Fig. S1 [56]). We note that

even though the low and high temperature phases of LSMO with the La:Sr ratio of 0.7:0.3 formally are metallic, the phase transition is commonly referred to as a metal-insulator transition to emphasize the large resistance difference between the FM and PM phases. In the low-temperature FM phase, the devices exhibited a $\Delta R/R \sim 0.2\%$ AMR (Supplemental Material Fig. S2 [56]). Near $T_c$, the application of a high magnetic field induced CMR, $\Delta R/R \sim 23\%$ at 20 kOe (Supplemental Material Fig. S1 [56]). Overall, the equilibrium electrical and magnetic properties of the patterned devices were typical of LSMO thin films, indicating that the device fabrication had no noticeable influence on the chemical or structural quality of the synthesized films.

The application of a large voltage triggers the MIT in LSMO devices, which produces volatile low-to-high resistance switching. Figure 1(a) shows the switching measurement setup schematic. A voltage source and an ammeter (depicted on the left of the device) probed the *I-V* characteristics of the entire Hall bar. The recorded *I-V* curve [Fig. 1(b)] has an *N*-type negative differential resistance region, a part of the *I-V* curve with slope $dV/dI < 0$, which is a signature of the low-to-high resistance switching. The switching is volatile: turning off the applied voltage automatically restores the initial low-resistance state. MIT switching in LSMO occurs in a characteristic spatial pattern: the formation of a localized high-resistance barrier perpendicular to the electric current flow [50], in contrast to the conventional conducting filament percolation along the current [57–59]. Two independent voltmeters [shown on the right of the device in Fig. 1(a)] monitored the local voltages across the two Hall bar sections, which allowed electrical probing of the barrier formation [Fig. 1(c)]. Initially as the applied voltage $V_{apl}$ is ramped up, the local voltages, $V_1$ and $V_2$, are nearly equal and increase monotonically. When the MIT is triggered and the high-resistance barrier forms at $V_{apl} \sim 14.5$ V, the local voltage $V_1$ [top Hall bar section in Fig. 1(a)] abruptly increases because the barrier acts as a voltage divider focusing a large fraction of the applied voltage on itself. Consequently, the local voltage $V_2$ across the metallic Hall bar section [bottom section in Fig. 1(a)] decreases abruptly. By comparing $V_1$ and $V_2$, it is always possible to unambiguously identify which section of the Hall bar, top or bottom, undergoes the electrically triggered MIT and which section remains in the metallic state.

*In-operando* magneto-optical Kerr effect (MOKE) imaging confirmed that the abrupt increase/decrease of $V_1/V_2$ is a direct consequence of the high-resistance PM barrier formation. The imaging procedure (details can be found elsewhere [50]) mapped the spatial distribution of the FM regions. Because the MIT and FM transitions in LSMO are coupled [60], the MOKE maps reveal the device areas that locally undergo MIT switching (areas where the MOKE signal vanishes) and the areas that remain in the FM metal state (areas where the MOKE signal is strong). The left panel in Fig. 1(d) shows a MOKE map acquired at $V_{apl} = 10$ V, i.e., a voltage that does not trigger the MIT. The entire device is uniformly FM implying that LSMO is in the metallic state. At $V_{apl} = 15$ V [Fig. 1(d), right panel], the MOKE map shows that the FM signal vanishes in the top Hall bar section. The map directly identifies the area where LSMO locally undergoes the phase transition and reveals that this phase transition results in the

formation of a high-resistance PM phase barrier, i.e., a region that stretches across the full device width and impedes the current flow. The barrier appears in the same section where the local voltage $V_1$ abruptly increases in the switching *I-V* measurements [Fig. 1(c)]. Because the transverse barrier is not expected to produce significant longitudinal current flow inhomogeneities, the total current and local voltages $V_1$ and $V_2$ can be used to calculate the effective resistances of the two Hall bar sections. Such simple local resistance calculations are justified when the switching occurs by the transverse barrier formation, while a different approach is needed when the switching causes a longitudinal filamentary percolation, which inevitably leads to a highly nonuniform current distribution [61].

## III. ANISOTROPIC MAGNETORESISTANCE

Intuitively, one might expect that the AMR will be suppressed when the applied voltage triggers the MIT because part of the device is in the PM phase and there is no AMR in the PM phase in thermal equilibrium (Supplemental Material Fig. S2 [56]). Contrary to this expectation, we found that triggering the MIT leads to a strong magnetoresistance anomaly. Figure 2(b) compares the AMR of the LSMO device under equilibrium conditions ($V_{apl} = 0.1$ V) and during resistive switching ($V_{apl} = 14.5$ V). The measurements were performed at 100 K and in 1-kOe magnetic field sufficient to saturate the magnetization in any in-plane direction. In equilibrium, the device shows conventional $\Delta R \sim \sin^2\varphi$ AMR behavior with the magnitude of $(R_\perp - R_{||})/R_{||} \sim +0.2\%$, where $R_\perp$ and $R_{||}$ are the resistances when the magnetization is saturated in the in-plane direction perpendicular or parallel to the electric current, respectively [Fig. 2(a)]. When applied voltage triggers the MIT at 14.5 V [Fig. 2(c)], the AMR magnitude in the Hall bar section that remains in the FM state increases by a factor of $\sim 8$ reaching $(R_\perp - R_{||})/R_{||} \sim +1.6\%$. In the Hall bar section that has the PM barrier, the AMR magnitude also increases and, surprisingly, flips sign becoming $(R_\perp - R_{||})/R_{||} \sim -1.9\%$. The two $R(\varphi)$ curves (FM metal and PM barrier sections) appear nearly as mirror reflections of each other. This reciprocal symmetry of the $R(\varphi)$ curves is an indication that the coupling between the two Hall bar sections during the MIT switching, i.e., the resistance change of one section is reflected in the other section, is responsible for the anomalous magnetotransport properties, as discussed later in the paper.

The AMR anomaly develops abruptly at the MIT triggering threshold voltage. Figure 2(d) shows the voltage dependence of AMR magnitude of the two Hall bar sections, one that undergoes switching into the high-resistance PM state (red curve) and the other one that remains in the FM metal state (blue curve). Before the switching is induced at 14.5 V, the AMR in both sections is equal and decreases slightly with increasing voltage, which most likely originates from uniform Joule heating that precedes the switching [50]. A sharp peak and the sign flip of $(R_\perp - R_{||})/R_{||}$ in the barrier section coincides with the threshold voltage that triggers the switching and causes the high-resistance PM barrier formation. At the threshold voltage, the barrier is the narrowest [50]. As the voltage increases, the barrier width grows and, simultaneously, the magnitude of the AMR anomaly decreases. The
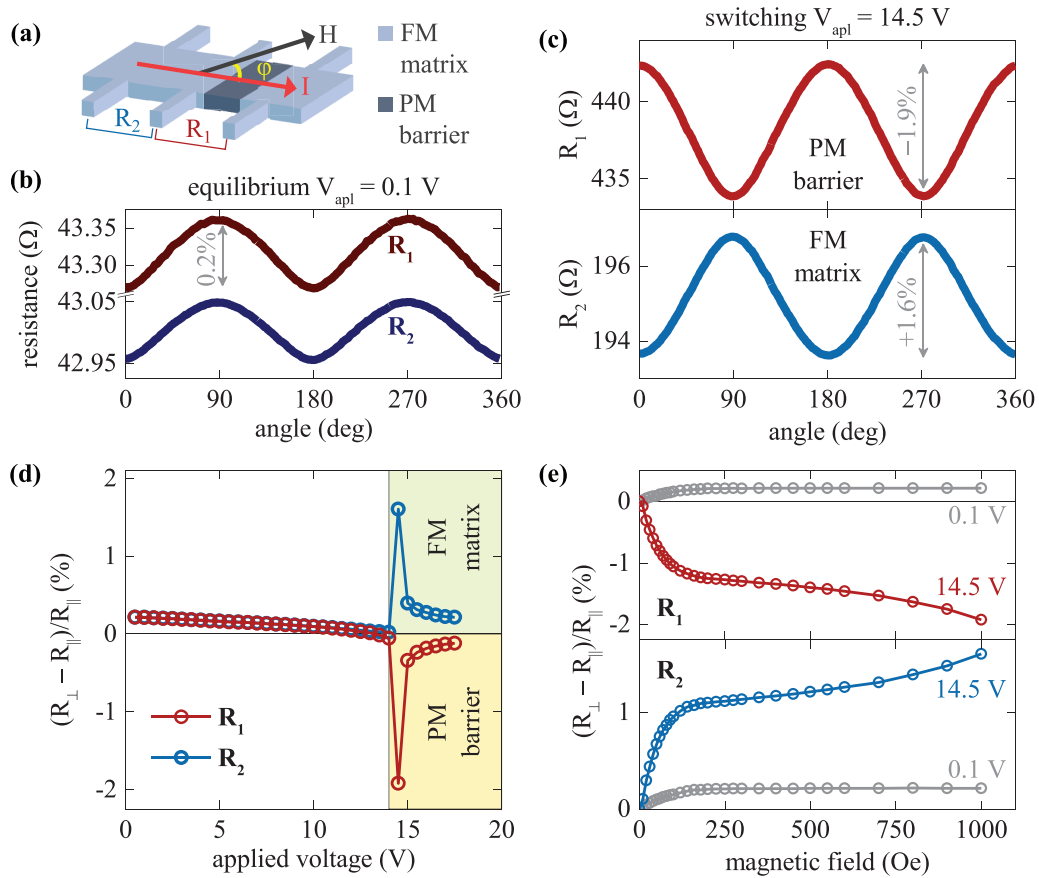
FIG. 2. (a) Schematic of the AMR measurement setup. (b) Resistance-angle curves in equilibrium (0.1 V) showing the AMR of $\Delta R/R \sim$ 0.2%. (c) Resistance-angle curves recorded at the MIT triggering threshold (14.5 V) in the Hall bar sections containing the PM barrier (top) and in the FM section (bottom). The AMR magnitude increases and its sign flips in the PM barrier section. (d) AMR magnitude as a function of applied voltage. The AMR anomaly can be observed at the MIT triggering threshold. AMR measurements in (b)–(d) were performed in 1-kOe applied field. (e) AMR amplitude dependence on the applied magnetic field in equilibrium (gray lines) and at the MIT triggering threshold (red and blue lines) for the PM barrier (top) and FM metal (bottom) Hall bar sections. At the switching, the AMR amplitude shows a persistent increase with increasing field. All measurements were done at 100 K.

sign flip of $(R_\perp - R_{||})/R_{||}$, however, persists in the PM barrier section as long as the device is in the switched state. When the applied voltage is turned off, the thermal equilibrium AMR properties are automatically restored because the MIT switching in LSMO is volatile.

Electrical MIT triggering in LSMO is mediated by Joule heating [50]. Even though the switching process is thermal in nature, the AMR magnitude voltage dependence drastically differs from the equilibrium temperature dependence [compare Fig. 2(d) and Supplemental Material Fig. S2 [56]]: (1) the equilibrium AMR magnitude never exceeds 0.25%, while the AMR reaches ~1.9% during switching, (2) $R_\perp > R_{||}$ at any temperature in equilibrium, while $R_\perp < R_{||}$ in the PM barrier section during switching. These two facts highlight the importance of the voltage induced PM barrier formation in the emergence of the magnetoresistance anomaly.

AMR is expected to be independent of the applied magnetic field magnitude provided that the field is sufficient to saturate the magnetization along all in-plane directions. This expectation is indeed satisfied in the LSMO devices in equilibrium, e.g., $(R_\perp - R_{||})/R_{||}$ has the same value of ~0.2% at 200 Oe and at 1000 Oe fields [Fig. 2(e), gray lines]. During

the switching, the AMR magnitude increases monotonically with increasing magnetic field without any signs of saturation [Fig. 2(e), red and blue lines]. Because the AMR anomaly is largest near the MIT triggering voltage [Fig. 2(d)], the absence of AMR saturation is likely an indication that the applied magnetic field drives the LSMO toward the state close to the switching threshold, i.e., when the barrier is narrowest, which could be due to a CMR mediated voltage/power redistribution, as discussed later in the paper.

Small-field magnetoresistance measurements showed evidence of the magnetic anisotropy change when the LSMO device undergoes the MIT switching. Figure 3 compares the resistance-field curves acquired with the magnetic field parallel, $R_{||} - H$, and perpendicular, $R_\perp - H$, to the electric current. A linear CMR contribution was subtracted from the $R$-$H$ curves in order to highlight the anisotropy related effects. Raw magnetoresistance data are shown in Supplemental Material Fig. S3 [56]. In equilibrium, the $R_{||} - H$ and $R_\perp - H$ curves (Fig. 3, grey lines) have opposite signs due to the intrinsic AMR. Both $R$-$H$ curves, however, have similar shapes and comparable magnitudes (~0.1%), which is indicative of the conventional easy-plane magnetic anisotropy in a thin
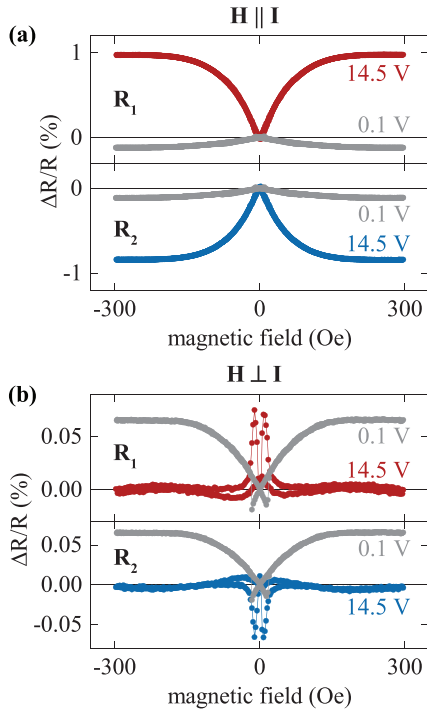
FIG. 3. Small-field magnetoresistance measurements with the magnetic field parallel (a) and perpendicular (b) to the electric current in equilibrium (0.1 V, gray lines) and at the MIT triggering threshold voltage (14.5 V, red and blue lines) corresponding to the two sections of the Hall bar device, $R_1$ and $R_2$ [defined in Fig. 2(a)]. During resistive switching, the magnetoresistance of the PM barrier section ($R_1$) flips sign. The shape and magnitude differences between $R_\parallel$-$H$ and $R_\perp$-$H$ curves indicate the change of magnetic anisotropy during the switching. All measurements were performed at 100 K.



FIG. 4. (a) Large-field magnetoresistance measurements at the MIT triggering threshold voltage (14.5 V). The $R$-$H$ curve of the PM barrier section of the Hall bar (top, red line) exhibits conventional negative CMR. The $R$-$H$ curve of the FM metal section shows an anomalous positive CMR. (b) Magnetoresistance at 20-kOe field as a function of the applied voltage. Similar to AMR in Fig. 2, CMR shows a strong anomaly at the MIT threshold triggering voltage. $R_1$ and $R_2$ notations are defined in Fig. 2(a). All measurements were performed at 100 K.

film. When the applied voltage triggers the MIT, the $R$-$H$ curves of the FM metal and PM barrier Hall bar sections (Fig. 3, red and blue lines) have the opposite signs consistent with the AMR sign flip discussed in the previous paragraphs [Figs. 2(c)–2(e)]. Importantly, the $R_\parallel - H$ and $R_\perp - H$ curves differ drastically in terms of shape and magnitude during the switching. The $R_\parallel$-$H$ curve displays a gradual evolution without distinct magnetization reversal features, and it has the large magnitude of ∼1%. Conversely, the magnetization reversal events are strongly pronounced in the $R_\perp - H$ curves, while $R_\perp$ has nearly the same value at remanence (zero field) and at the maximum applied field (300 Oe). The observed differences between the $R_\parallel - H$ and $R_\perp - H$ curves suggest that during the switching, the magnetization prefers the direction perpendicular to the current (i.e., aligned with the transverse PM barrier), consistent with our recent MOKE studies of the uniaxial anisotropy development in the LSMO switching devices [52].

## IV. COLOSSAL MAGNETORESISTANCE

An anomaly coinciding with the electrical triggering of MIT can be also observed in the high-field CMR measurements. In equilibrium, the application of a high magnetic field reinforces the FM metal phase in LSMO, which leads to a large (i.e., colossal) resistance decrease (negative
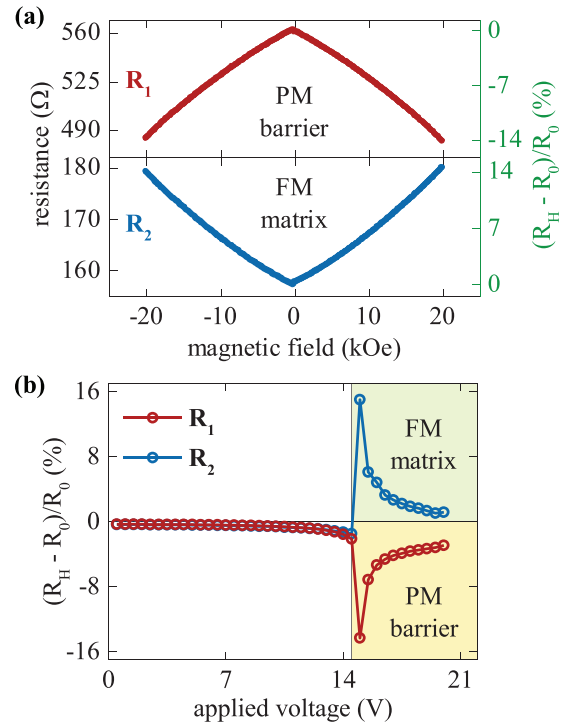
magnetoresistance) near the phase transition temperature [60]. Because the electrical MIT triggering in LSMO is mediated by Joule heating [50], it may be expected that the regions near the PM barrier will locally exhibit a CMR as their temperature is close to $T_c$, while the magnetoresistance will be small in the FM regions as their temperature is far below $T_c$. Contrary to the expectations, we observed a strong magnetoresistance response both in the PM barrier and FM metal Hall bar sections during the switching (Fig. 4). Magnetoresistance in the PM barrier section is negative, reaching −15% at 20-kOe field [Fig. 4(a), top panel]. This PM barrier magnetoresistance is comparable to the equilibrium CMR at $T_c$, −15% vs −23%, respectively, although only a small volume fraction of the device is expected to be close to $T_c$ at the switching threshold voltage, while the entire material volume contributes to the equilibrium CMR.

Surprisingly, the FM metal section also exhibits an anomalous CMR-like effect, but its magnetoresistance is positive, +15% [Fig. 4(a), bottom panel]. We note that although the relative magnetoresistance values of the PM barrier and FM sections have nearly equal magnitudes, −15% vs +15%, the absolute resistances differ by the factor of ∼3, allowing the unambiguous identification of the Hall bar section that undergoes the MIT switching. The two $R$-$H$ curves (PM barrier and FM metal) appear nearly as mirror reflections of
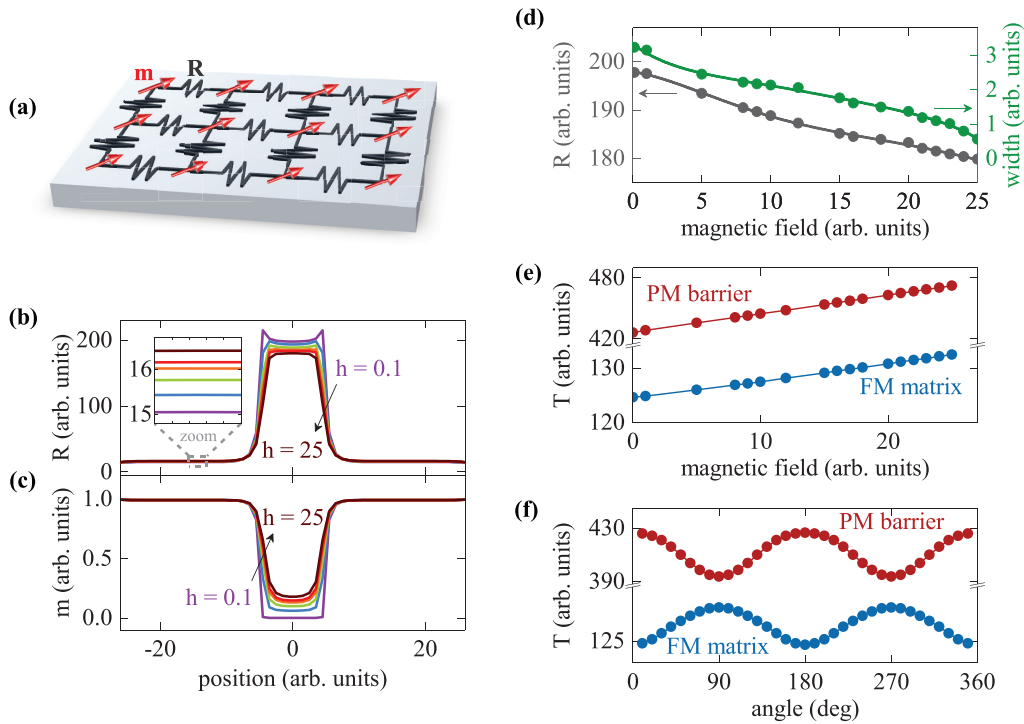
FIG. 5. (a) Schematic of the hybrid resistor network + Ising model. (b), (c) Magnetic field dependence of the resistance (b) and magnetization profiles (c) across the switching device length at an applied voltage above the MIT triggering threshold. The formation of a high-resistance PM barrier at the device center is clearly visible. The inset in (b) shows a zoom-in of the resistance profile in a metallic region of the device. The resistance of the metallic regions increases with increasing magnetic field, which yields a positive magnetoresistance. (d) Magnetic field dependence of the resistance (black curve) and width (green curve) of the PM barrier. (e) Temperature of the PM barrier (red curve) and metallic matrix (blue curve) as a function of the magnetic field. (f) Temperature of the PM barrier (red curve) and metallic matrix (blue curve) as a function of the angle between the magnetization and current.

each other, which suggests that interaction between the low-resistance FM and high-resistance PM regions is responsible for the anomalous CMR properties, similar to the previously discussed AMR anomaly.

The strongest CMR anomaly occurs at the MIT triggering threshold [Fig. 4(b)]. At the threshold voltage, the *I-V* curve has the sharpest slope [Fig. 1(b)] corresponding to a rapid resistance change, i.e., the resistive switching. Consequently, even a small external stimulus that influences the power/voltage distribution balance in the device can drive a large resistive change response. As we discuss in Sec. V, the resistance modulation associated with the intrinsic AMR and CMR can couple with the resistive switching process, which leads to an emergent magnetoresistance anomaly.

## V. SWITCHING MODEL

To investigate the possible mechanism behind the observed AMR and CMR anomalies, we developed a hybrid model by combining a resistive network with the Ising model [Fig. 5(a)]. The value of each resistor in the network depends on magnetization *m* and temperature *T*:

$$R(m, T) = R_0 T e^{\varepsilon\left[(1-m^2)/T\right]}, \quad (1)$$

where $R_0$ and $\varepsilon$ are constants. Equation (1) was found to provide a good phenomenological description of the MIT and CMR in rare-earth manganites [62,63]. In the simulations, we

set the applied voltage and magnetic field and we solve the resistor network by considering electrothermal effects [50,61]. Using local temperature, we compute local magnetization from the mean-field Ising model solution:

$$m = \tanh\frac{h + T_c m}{T}, \quad (2)$$

where *h* is the magnetic field and $T_c$ is the critical temperature. The obtained local magnetization and temperature are then used to update the resistor values in the network. For each applied voltage and field, we ran an iterative process until all variables converged.

Similar to the experimental results [Fig. 1(d)], the model shows that the switching occurs by the formation of a high-temperature PM resistive barrier inside the low-temperature FM metal matrix [Figs. 5(b) and 5(c)]. The model further yields that the PM barrier's resistance and size depend on the applied magnetic field [Fig. 5(d)]. As the field increases, the PM barrier region (whose temperature is just above $T_c$) develops a noticeable magnetization [Fig. 5(c)], leading to a resistance decrease given by Eq. (1), i.e., the intrinsic CMR. This resistance decrease in the high-temperature PM barrier region lowers the total resistance of the entire device causing the power dissipation and temperature increase because the device is under a constant applied voltage [Fig. 5(e)]. As the PM barrier temperature is close to $T_c$, the intrinsic CMR produces a larger resistance change compared to the effect of

the temperature change induced by the applied magnetic field, which explains the negative magnetoresistance of the PM barrier Hall bar section observed in the experiments (Fig. 4). The temperature of the FM metal matrix, on the other hand, is much lower than $T_c$. The FM metal matrix, consequently, does not exhibit a noticeable intrinsic CMR leaving the magnetic field induced temperature increase as the primary factor determining the resistance of these regions. Due to the positive resistance-temperature dependence in the FM metal state, its resistance increases with magnetic field [inset in Fig. 5(b)], which explains the positive magnetoresistance of the FM metal Hall bar section observed in the experiments (Fig. 4).

To explore the effect of AMR during the switching, we explicitly introduced the resistance angular dependence on the magnetization direction into Eq. (1) by setting

$$R_0(\varphi) = R_{||} + (R_\perp - R_{||})\sin^2\varphi. \tag{3}$$

We fit the experimental AMR data (Suppl. Fig. 2) [56] to obtain the temperature-dependent $R_{||}$ and $R_\perp$ values used in the simulations. The model revealed that in the switched state, the temperature of both the FM metal matrix and high-resistance PM barrier depends on the magnetization direction [Fig. 5(f)]. This angular dependence of temperature can be understood as follows. The FM metal matrix has the intrinsic positive AMR, i.e., its resistance is maximized when the magnetization is perpendicular to the current ($R_\perp > R_{||}$). In the resistive switching state, a small AMR-induced resistance increase leads to an increase of the dissipated power (hence, the temperature increase) in the FM metal region because of voltage focusing. As the AMR initiates the voltage/power focusing, this focusing is further amplified by the natural positive resistance-temperature dependence in the FM metal state. Thus, the combined effect of the intrinsic AMR and resistance-temperature dependence can explain the effective AMR increase in the metallic section of the Hall bar observed in the experiments (Figs. 2 and 3). On the other hand, as the FM metal regions focus more dissipated power, the temperature of the PM barrier section decreases [Fig. 5(f)] and, consequently, its resistance also decreases. This decrease in resistance produces an apparent negative AMR observed in the PM barrier section (Fig. 2) even though the barrier itself is in the PM state and does not have an intrinsic AMR.

Overall, the model shows that the coupling between the intrinsic magnetoresistance and resistive switching state leads to anomalous CMR and AMR behavior not found in the thermal equilibrium state. During the electrical triggering of MIT, a phase separation pattern of the high- and low-resistance regions emerges. The size and temperature of these regions are highly susceptible to the influence of external stimuli because the phase separation pattern depends on a delicate voltage/power distribution balance in the device. Even a small resistance change produced by the intrinsic magnetoresistance can significantly alter this balance resulting in the temperature and size change of the high- and low-resistance regions. An effective magnetoresistance amplification can be achieved when the intrinsic magnetoresistance and voltage/power redistribution act together, i.e., both effects cause a resistance change in the same direction. Our model shows that this amplification is an apparent nonequilibrium phenomenon that stems from the interplay between the intrinsic AMR/CMR and resistive switching state. Such an effective magnetoresistance amplification does not directly require a change of the intrinsic properties that define the intrinsic magnetoresistance response, e.g., spin-orbit coupling or double exchange interactions, even though the contribution of intrinsic property change during the MIT switching in LSMO devices cannot be completely ruled out in our experiments. Because our model incorporates only the most general features of LSMO (MIT and intrinsic AMR/CMR), the observed magnetoresistance anomalies are likely not unique to LSMO as a specific material but may represent a general phenomenon in magnetic MIT switching systems.

## VI. CONCLUSION

This work reports an anomalous magnetoresistance behavior in LSMO devices when the material is driven into the resistive switching state. At the MIT triggering threshold voltage, both the AMR and CMR show a large increase in magnitude. Surprisingly, an effective AMR increase and a sign flip can be observed in the device regions switched into the high-resistance PM phase even though the PM phase does not have an AMR in equilibrium. The cold FM metal matrix surrounding the hot switched regions has a strong positive CMR response, in stark contrast to the intrinsic negative CMR that only appears near $T_c$ under equilibrium conditions. We attribute the above effects to the coupling between the intrinsic magnetoresistance and voltage/power distribution in the resistive switching state. This coupling enables the size and temperature control of the high/low-resistance regions by applying an external magnetic field. The key feature producing the magnetoresistance anomaly is the emergence of a characteristic high/low-resistance phase separation pattern during the electrical MIT triggering, specifically for LSMO, the formation of a high-resistance PM barrier that splits the FM metal matrix. Percolating filaments or blocking barriers are commonly observed in resistive switching devices [50,58,59]. Therefore, it can be expected that unusual magnetotransport phenomena might be also found in a variety of magnetically ordered MIT switching systems, such as other magnetic members of the rare-earth manganite family [45,60], antiferromagnetic rare-earth nickelates [64,65], ferrimagnetic $Fe_3O_4$ [66,67], and antiferromagnetic $V_2O_3$ [58,68].

[1] D. Ielmini and H.-S. P. Wong, In-memory computing with resistive switching devices, Nat. Electron. **1**, 333 (2018).

[2] J. Grollier, D. Querlioz, K. Y. Camsari, K. Everschor-Sitte, S. Fukami, and M. D. Stiles, *Neuromorphic Spintronics*, Nat. Electron. **3**, 360 (2020).

[3] A. Hoffmann, S. Ramanathan, J. Grollier, A. Kent, M. Rozenberg, I. Schuller, O. Shpyrko, R. Dynes, Y. Fainman, A. Frano *et al.*, Quantum materials for energy-efficient neuromorphic computing: Opportunities and challenges, APL Mater. **10**, 070904 (2022).

[4] J. del Valle, J. G. Ramírez, M. J. Rozenberg, and I. K. Schuller, Challenges in materials and devices for resistive-switching-based neuromorphic computing, J. Appl. Phys. **124**, 211101 (2018).

[5] A. Hirohata, K. Yamada, Y. Nakatani, I.-L. Prejbeanu, B. Diény, P. Pirro, and B. Hillebrands, Review on spintronics: Principles and device applications, J. Magn. Magn. Mater. **509**, 166711 (2020).

[6] K. Sun, J. Chen, and X. Yan, The future of memristors: Materials engineering and neural networks, Adv. Funct. Mater. **31**, 2006773 (2021).

[7] B. Mohammad, M. A. Jaoude, V. Kumar, D. M. Al Homouz, H. A. Nahla, M. Al-Qutayri, and N. Christoforou, State of the art of metal oxide memristor devices, Nanotechnol. Rev. **5**, 311 (2016).

[8] P. Krzysteczko, G. Reiss, and A. Thomas, Memristive switching of mgo based magnetic tunnel junctions, Appl. Phys. Lett. **95**, 112508 (2009).

[9] A. Sokolov, R. Sabirianov, I. Sabirianov, and B. Doudin, Voltage-induced switching with magnetoresistance signature in magnetic nano-filaments, J. Phys.: Condens. Matter **21**, 485303 (2009).

[10] P. Krzysteczko, J. Münchenberger, M. Schäfers, G. Reiss, and A. Thomas, The memristive magnetic tunnel junction as a nanoscopic synapse-neuron system, Adv. Mater. **24**, 762 (2012).

[11] R. Göckeritz, N. Homonnay, A. Müller, B. Fuhrmann, and G. Schmidt, Resistive switching and voltage induced modulation of tunneling magnetoresistance in nanosized perpendicular organic spin valves, AIP Adv. **6**, 45003 (2016).

[12] X. Li, J. Jia, Y. Li, Y. Bai, J. Li, Y. Shi, L. Wang, and X. Xu, Realization of resistive switching and magnetoresistance in ZnO/ZnO-Co composite materials, Sci. Rep. **6**, 31934 (2016).

[13] J. Jeon, J. Jung, and K. H. Chow, Coexistence of non-volatile Bi-Polar resistive switching and tunneling magnetoresistance in spatially confined $La_{0.3}Pr_{0.4}Ca_{0.3}MnO_3$ Films, Appl. Phys. Lett. **111**, 242401 (2017).

[14] D. Zhao, S. Qiao, Y. Luo, A. Chen, P. Zhang, P. Zheng, Z. Sun, M. Guo, F. Chiang, J. Wu *et al.*, Magnetoresistance behavior of conducting filaments in resistive-switching NiO with different resistance states, ACS Appl. Mater. Interfaces **9**, 10835 (2017).

[15] G. Chen, C. Song, C. Chen, S. Gao, F. Zeng, and F. Pan, Resistive switching and magnetic modulation in cobalt-doped ZnO, Adv. Mater. **24**, 3515 (2012).

[16] S. Ren, H. Qin, J. Bu, G. Zhu, J. Xie, and J. Hu, Coexistence of electric field controlled ferromagnetism and resistive switching for $TiO_2$ film at room temperature, Appl. Phys. Lett. **107**, 62404 (2015).

[17] F. Du, Y. Li, X. Li, J. Yang, Y. Bai, Z. Quan, C. Liu, and X. Xu, Resistive switching and its modulating ferromagnetism and magnetoresistance of a ZnO-Co/$SiO_2$-Co film, J. Magn. Magn. Mater. **489**, 165445 (2019).

[18] L. Wei, Z. Hu, G. Du, Y. Yuan, J. Wang, H. Tu, B. You, S. Zhou, J. Qu, H. Liu *et al.*, Full electric control of exchange bias at room temperature by resistive switching, Adv. Mater. **30**, 1801885 (2018).

[19] Y. Yuan, J. Qu, L. Wei, R. Zheng, Y. Lu, R. Liu, T. Liu, J. Chen, L. Luo, G. Du *et al.*, Electric control of exchange bias at room temperature by resistive switching via electrochemical metallization, ACS Appl. Mater. Interfaces **14**, 26941 (2022).

[20] X. Zhu, J. Zhou, L. Chen, S. Guo, G. Liu, R. W. Li, and W. D. Lu, *In* Situ nanoscale electric field control of magnetism by nanoionics, Adv. Mater. **28**, 7658 (2016).

[21] Y. Ahn and J. Y. Son, Conductive filament nanostructures and their magnetization reversal in NiO resistive switching memory cells, Mater. Sci. Eng. B: Solid-State Mater. Adv. Technol. **283**, 115816 (2022).

[22] P. Stoliar, L. Cario, E. Janod, B. Corraze, C. Guillot-Deudon, S. Salmon-Bourmand, V. Guiot, J. Tranchant, and M. Rozenberg, Universal electric-field-driven resistive transition in narrow-gap Mott insulators, Adv. Mater. **25**, 3222 (2013).

[23] J. S. Brockman, L. Gao, B. Hughes, C. T. Rettner, M. G. Samant, K. P. Roche, and S. S. P. Parkin, Subnanosecond incubation times for electric-field-induced metallization of a correlated electron oxide, Nat. Nanotechnol. **9**, 453 (2014).

[24] Y. Kalcheim, A. Camjayi, J. del Valle, P. Salev, M. Rozenberg, and I. K. Schuller, Non-thermal resistive switching in Mott insulator nanowires, Nat. Commun. **11**, 2985 (2020).

[25] J. Park, T. Hadamek, A. B. Posadas, E. Cha, A. A. Demkov, and H. Hwang, Multi-layered $NiO_y$/$NbO_x$/$NiO_y$ fast drift-free threshold switch with high Ion/Ioff ratio for selector application, Sci. Rep. **7**, 4068 (2017).

[26] M. Son, J. Lee, J. Park, J. Shin, G. Choi, S. Jung, W. Lee, S. Kim, S. Park, and H. Hwang, Excellent selector characteristics of nanoscale $VO_2$ for high-density bipolar reram applications, IEEE Electron Device Lett. **32**, 1579 (2011).

[27] M. Liu, H. Hwang, H. Tao, A. Strikwerda, K. Fan, G. Keiser, A. Sternbach, K. West, S. Kittiwatanakul, J. Lu *et al.*, Terahertz-field-induced insulator-to-metal transition in vanadium dioxide metamaterial, Nature (London) **487**, 345 (2012).

[28] N. Butakov, M. Knight, T. Lewi, P. Iyer, D. Higgs, H. Chorsi, J. Trastoy, J. del Valle, I. Valmianski, C. Urban *et al.*, Broadband electrically tunable dielectric resonators using metal-insulator transitions, ACS Photonics **5**, 4056 (2018).

[29] S. Yang, M. Vaseem, and A. Shamim, Fully inkjet-printed $VO_2$-based radio-frequency switches for flexible reconfigurable components, Adv. Mater. Technol. **4**, 1800276 (2019).

[30] M. D. Pickett, G. Medeiros-Ribeiro, and R. S. Williams, A scalable neuristor built with Mott memristors, Nat. Mater. **12**, 114 (2013).

[31] W. Yi, K. K. Tsang, S. K. Lam, X. Bai, J. A. Crowell, and E. A. Flores, Biological plausibility and stochasticity in scalable $VO_2$ active memristor neurons, Nat. Commun. **9**, 4661 (2018).

[32] J. del Valle, P. Salev, Y. Kalcheim, and I. K. Schuller, A caloritronics-based Mott neuristor, Sci. Rep. **10**, 4292 (2020).

[33] C. Adda, M. Lee, Y. Kalcheim, P. Salev, R. Rocco, N. Vargas, N. Ghazikhanian, C. Li, G. Albright, M. Rozenberg, and

I. Schuller, Direct observation of the electrically triggered insulator-metal transition in $V_3O_5$ far below the transition temperature, Phys. Rev. X **12**, 011025 (2022).

[34] J. del Valle, P. Salev, S. Gariglio, Y. Kalcheim, I. K. Schuller, and J.-M. Triscone, Generation of tunable stochastic sequences using the insulator–metal transition, Nano Lett. **22**, 1251 (2022).

[35] E. Qiu, P. Salev, L. Fratino, R. Rocco, H. Navarro, C. Adda, J. Li, M. Lee, Y. Kalcheim, M. Rozenberg, and I. Schuller, Stochasticity in the synchronization of strongly coupled spiking oscillators, Appl. Phys. Lett. **122**, 94105 (2023).

[36] T. Driscoll, H.-T. Kim, B.-G. Chae, M. Di Ventra, and D. N. Basov, Phase-transition driven memristive system, Appl. Phys. Lett. **95**, 43503 (2009).

[37] L. Pellegrino, N. Manca, T. Kanki, H. Tanaka, M. Biasotti, E. Bellingeri, A. S. Siri, and D. Marré, Multistate memory devices based on free-standing $VO_2/TiO_2$ microstructures driven by joule self-heating, Adv. Mater. **24**, 2929 (2012).

[38] S. Bae, S. Lee, H. Koo, L. Lin, B. H. Jo, C. Park, and Z. L. Wang, The memristive properties of a single $VO_2$ nanowire with switching controlled by self-heating, Adv. Mater. **25**, 5098 (2013).

[39] N. Vardi, E. Anouchi, T. Yamin, S. Middey, M. Kareev, J. Chakhalian, Y. Dubi, and A. Sharoni, Ramp-reversal memory and phase-boundary scarring in transition metal oxides, Adv. Mater. **29**, 1605029 (2017).

[40] S. Basak, Y. Sun, M. A. Banguero, P. Salev, I. K. Schuller, L. Aigouy, E. W. Carlson, and A. Zimmers, Spatially distributed ramp reversal memory in $VO_2$, Adv. Electron. Mater. **9**, 2300085 (2023).

[41] M. Liu, J. Hoffman, J. Wang, J. Zhang, B. Nelson-Cheeseman, and A. Bhattacharya, Non-volatile ferroelastic switching of the verwey transition and resistivity of epitaxial $Fe_3O_4$/PMN-PT (011), Sci. Rep. **3**, 1876 (2013).

[42] P. Salev, J. del Valle, Y. Kalcheim, and I. K. Schuller, Giant nonvolatile resistive switching in a Mott oxide and ferroelectric hybrid, Proc. Natl. Acad. Sci. **116**, 8798 (2019).

[43] M. Imada, A. Fujimori, and Y. Tokura, Metal-insulator transitions, Rev. Mod. Phys. **70**, 1039 (1998).

[44] A. Asamitsu, Y. Tomioka, H. Kuwahara, and Y. Tokura, Current switching of resistive states in magnetoresistive manganites, Nature (London) **388**, 50 (1997).

[45] M. Tokunaga, Y. Tokunaga, and T. Tamegai, Imaging of percolative conduction paths and their breakdown in phase-separated $(La_{1-y}Pr_y)_{0.7}Ca_{0.3}MnO_3$ with Y = 0.7, Phys. Rev. Lett. **93**, 037203 (2004).

[46] A. Molinari, H. Hahn, and R. Kruk, Voltage-controlled on/off switching of ferromagnetism in manganite supercapacitors, Adv. Mater. **30**, 1703908 (2018).

[47] C. Thiele, K. Dörr, O. Bilani, J. Rödel, and L. Schultz, Influence of strain on the magnetization and magnetoelectric effect in $La_{0.7}A_{0.3}MnO_3$/PMN_PT(001) (A = Sr, Ca), Phys. Rev. B **75**, 054408 (2007).

[48] L. Liu, G. Zhou, X. Shu, C. Li, W. Lin, L. Ren, C. Zhou, T. Zhao, R. Guo, Q. Xie et al., Room-temperature spin-orbit torque switching in a manganite-based heterostructure, Phys. Rev. B **105**, 144419 (2022).

[49] S. Guénon, S. Scharinger, S. Wang, J. G. Ramírez, D. Koelle, R. Kleiner, and I. K. Schuller, Electrical breakdown in a $V_2O_3$ device at the insulator-to-metal transition, Europhys. Lett. **101**, 57003 (2013).

[50] P. Salev, L. Fratino, D. Sasaki, R. Berkoun, J. del Valle, Y. Kalcheim, Y. Takamura, M. Rozenberg, and I. K. Schuller, Transverse barrier formation by electrical triggering of a metal-to-insulator transition, Nat. Commun. **12**, 5499 (2021).

[51] T. Z. Ward, J. D. Budai, Z. Gai, J. Z. Tischler, L. Yin, and J. Shen, Elastically driven anisotropic percolation in electronic phase-separated manganites, Nat. Phys. **5**, 885 (2009).

[52] P. Salev, I. Volvach, D. Sasaki, P. Lapa, Y. Takamura, V. Lomakin, and I. K. Schuller, Voltage-controlled magnetic anisotropy enabled by resistive switching, Phys. Rev. B **107**, 054415 (2023).

[53] E. Dagotto, *Nanoscale Phase Separation and Colossal Magnetoresistance* (Springer, Berlin, 2003), Vol. 136.

[54] R. V. Chopdekar, B. Li, T. A. Wynn, M. S. Lee, Y. Jia, Z. Q. Liu, M. D. Biegalski, S. T. Retterer, A. Young, A. Scholl, and Y. Takamura, Nanostructured complex oxides as a route towards thermal behavior in artificial spin ice systems, Phys. Rev. Mater. **1**, 024401 (2017).

[55] D. Y. Sasaki, R. V. Chopdekar, S. T. Retterer, D. Y. Jiang, J. K. Mason, M. S. Lee, and Y. Takamura, Formation of complex spin textures in thermally demagnetized $La_{0.7}Sr_{0.3}MnO_3$ artificial-spin-ice structures, Phys. Rev. Appl. **17**, 064057 (2022).

[56] See Supplemental Material at http://link.aps.org/supplemental/10.1103/PhysRevB.108.174434 for additional experimental data.

[57] J. del Valle, N. Vargas, R. Rocco, P. Salev, Y. Kalcheim, P. Lapa, C. Adda, M. Lee, P. Wang, and I. Schuller, Spatiotemporal characterization of the field-induced insulator-to-metal transition, Science **373**, 907 (2021).

[58] M. Lange, S. Guénon, Y. Kalcheim, T. Luibrand, N. M. Vargas, D. Schwebius, R. Kleiner, I. K. Schuller, and D. Koelle, Imaging of electrothermal filament formation in a Mott insulator, Phys. Rev. Appl. **16**, 054027 (2021).

[59] T. Luibrand, A. Bercher, R. Rocco, F. Tahouni-Bonab, L. Varbaro, C. W. Rischau, C. Dominguez, Y. Zhou, W. Luo, S. Bag et al., Characteristic length scales of the electrically induced insulator-to-metal transition, Phys. Rev. Res. **5**, 013108 (2023).

[60] Y. Tokura, Critical features of colossal magnetoresistive manganites, Rep. Prog. Phys. **69**, 797 (2006).

[61] R. Rocco, J. del Valle, H. Navarro, P. Salev, I. K. Schuller, and M. Rozenberg, Exponential escape rate of filamentary incubation in Mott spiking neurons, Phys. Rev. Appl. **17**, 024028 (2022).

[62] J. Z. Wang, J. R. Sun, G. J. Liu, F. X. Hu, T. Y. Zhao, and B. G. Shen, A universal relation between resistivity and magnetization in paramagnetic state of manganites, Appl. Phys. Lett. **91**, 262506 (2007).

[63] H. Navarro, A. C. Basaran, F. Ajejas, L. Fratino, S. Bag, T. D. Wang, E. Qiu, V. Rouco, I. Tenreiro, F. Torres et al., Light-induced decoupling of electronic and magnetic properties in manganites, Phys. Rev. Appl. **19**, 044077 (2023).

[64] S. Catalano, M. Gibert, J. Fowlie, J. Íñiguez, J.-M. Triscone, and J. Kreisel, Rare-earth nickelates $RNiO_3$: Thin films and heterostructures, Rep. Prog. Phys. **81**, 46501 (2018).

[65] J. del Valle, R. Rocco, C. Domínguez, J. Fowlie, S. Gariglio, M. J. Rozenberg, and J.-M. Triscone, Dynamics of the electrically induced insulator-to-metal transition in rare-earth nickelates, Phys. Rev. B **104**, 165141 (2021).

[66] J. García and G. Subías, The verwey transition—a new perspective, J. Phys.: Condens. Matter **16**, R145 (2004).

[67] S. Lee, A. Fursina, J. T. Mayo, C. T. Yavuz, V. L. Colvin, R. G. S. Sofin, I. V. Shvets, and D. Natelson, Electrically driven phase transition in magnetite nanostructures, Nat. Mater. **7**, 130 (2007).

[68] J. Trastoy, A. Camjayi, J. del Valle, Y. Kalcheim, J. Crocombette, D. Gilbert, J. Borchers, J. Villegas, D. Ravelosona, M. J. Rozenberg, and I. Schuller, Magnetic field frustration of the metal-insulator transition in $V_2O_3$, Phys. Rev. B **101**, 245109 (2020).